# Supporting Information

## Solar-driven ionic power generation via a film of nanocellulose @ conductive metal-organic framework

Shengyang Zhou,[1] Zhen Qiu,[2] Maria Strømme,[1]* Chao Xu[1]*

[1]Nanotechnology and Functional Materials, Department of Materials Science and Engineering, The Ångström Laboratory, Uppsala University, 751 03 Uppsala, Sweden

[2]Solid State Physics, Department of Materials Science and Engineering, The Ångström Laboratory, Uppsala University, 751 03 Uppsala, Sweden

*Email: maria.stromme@angstrom.uu.se; chao.xu@angstrom.uu.se

## Experimental Methods

**Materials.** *Cladophora* cellulose (CC) was purchased from FMC Biopolymer (U.S.A.). 2,3,6,7,10,11-hexaiminotriphenylene (HITP) was purchased from Tensus Biotech (China). 2,2,6,6-tetramethylpiper-idine-1-oxyl (TEMPO) and nickel chloride ($NiCl_2$) were purchased from Sigma-Aldrich (Sweden).

**Preparation of CCM thin film**. CC was first treated by TEMPO oxidation to introduce carboxyls on the surface according to the previously reported method.[1] A solution of $NiCl_2$ with excessive $Ni^{2+}$ was added to the carboxylated-CC suspension (0.5 mg $mL^{-1}$), and the mixture was stirred for 2 h and then sonicated for 30 min. The gel of the $Ni^{2+}$-exchanged CC was then collected by filtration. Thereafter, a mixture solution of $NiCl_2$ (39 mg, 0.3 mmol) in 5 mL water and HITP·6HCl (107 mg, 0.2 mmol) in 20 mL $H_2O$ was added into a suspension of $Ni^{2+}$-exchanged CC (20 mL, 5 mg $ml^{-1}$). Then, an aqueous ammonia solution (1 mL, 14 mol $L^{-1}$) was added. The mixture was stirred at 70 °C for 1 h with an airflow and another 2 h without airflow. The obtained suspension was vacuum filtered on a PVDF membrane (pore size: 0.1 μm, Merck Millipore Ltd, Ireland) and washed by water and methanol. The freestanding CCM film can be pealed off from the PVDF membrane after drying the filter cake at 70 ℃ overnight. Detailed procedures are displayed in Fig. S1.

**Material characterizations**. TEM images were collected in a TEM instrument (Tecnai, AT02) at an accelerating voltage of 200 kV. SEM images were recorded on an FEG SEM instrument (Zeiss, Leo Gemini 1530) at an accelerating voltage of 3 kV. UV–vis–NIR absorption spectra were collected in a PerkinElmer Lambda 900 spectrometer.

Water contact angle was measured by a home-made equipment with a micro-focusing camera. Zeta potential was measured by a Zetasizer (Malvern). $N_2$ sorption isotherms were recorded in a surface area and pore size analyzer (Micromeritics ASAP 2020) at 77 K. The samples were degassed at 100 °C under a kinetic vacuum (<$10^{-5}$ mmHg) for 10 h before the measurements. Pore size distribution was calculated using the software package (Micro-meritics ASAP 2020). The electrical resistance of the CCM film was measured in a 4-point-probe station (Hewlett Packard 34401A). FTIR spectra were recorded in a Bruker Tensor 27 spectrometer with an attenuated total refection (ATR) mode. X-ray photoelectron spectroscopy (XPS) spectra were recorded by a PHI Quantera II instrument (Physical Electronics, USA). X-Ray diffraction patterns were recorded in a Bruker Focus D8 diffractometer with Cu Kα X-ray radiation. TGA measurement was carried out on a thermogravimetric analyzer (Mettler Toledo, /SDTA851e) under air flow with a heating rate of 10 °C $min^{-1}$.

**Solar thermal evaporation measurements and simulations**. The experiments of solar photothermal conversion and the induced water evaporation were carried out with a self-designed apparatus according to the reported standard method.[2] A 200 mL beaker was filled with 150 mL water. The CCM film was placed on a polystyrene sponge that was floated on the water surface, where two ends of the film are inserted into the water (Fig. 2b). A solar simulator (General Electric ELH Lamp 300W, 120V) with an intensity of one sun (the working distance was calibrated by a standard silicon *p-n* junction solar cell) was placed above the CCM film. The time-dependent mass of the whole aperture (including the beaker, water, film and sponge) was recorded by a balance (ME2002,

METTLER TOLEDO) and the surface temperature of the CCM film was recorded by an infrared thermal camera. TGA-DSC curves were recorded in a thermogravimetric analyzer (Mettler Toledo, SDTA851e). A piece of CCM film was cut into a disk with a diameter of 3.5 mm that fitted the size of the alumina crucible. The film was then placed on the surface of a cylindrical sponge full of water in the crucible (schematic in Fig. S5b). The temperature program was set according to the following: first equilibrating at 17 ℃, then temperature increase with a rate of 5 K $min^{-1}$ until 53 ℃ to simulate the experimental rate, finally the temperature was stable at 53 ℃ for 30 min (Fig. S5a). In this procedure, the mass and enthalpy were synchronously recorded (Fig. S5b). The water transport simulations were performed by COMSOL Multiphysics 5.4. The geometry was established according to a simplified model (Fig. S6). The package of laminar flow was chosen where the upper boundary was set as water loss with a rate of 0.67 μm $s^{-1}$.

**Ionic conduction measurements**. Ionic conductivity was measured by a home-made apertures (Fig. S7a-b). First, the CCM films were cut into rectangular pieces (0.2 cm × 0.5 cm). Then the CCM films were embedded in polydimethylsiloxane where two terminals were contacted with the electrolyte. Two symmetrical Ag/AgCl electrodes were immersed into the electrolyte. Bulk ionic conductivity $K$ was calculated by: $K = GL/Wd$, where $G$ is the measured conductance derived from the slope of the collected I−V curve, $L$ is the length, $W$ is the width, and $d$ is the thickness of the CCM film.[3] The calibration was carried out by measuring the conductivity of bulk electrolyte in different NaCl concentration ($10^{-5}$–$10^{0}$ M).

**Electrical characterizations in ionic power generation**. The CCM film was first cut into a rectangle shape, and then fixed on a quartz substrate. The I−V curves were recorded on by an electronic source meter (Hewlett Packard 34401A) equipped with four probes. To investigate the voltage contribution from various processes separately, different procedures were employed. The electrolytes with different salt concentration and pH value were dropped on one side of the CCM thin films to explore the streaming potential. An air blower was used to produce various water evaporation rates by adjusting the blowing rate (Fig. 4b). In order to measure the ionic thermoelectric voltage, an apparatus was designed by applying a temperature difference of 5 °C between two side of the CCM film (17 vs 22°C) infiltrated with electrolyte (0.01M NaCl, pH=10) and the film was sealed in a coffee-bag arrangement (Fig. S10). The potential difference between the warm and cold side was monitored by an electrochemical instrument (CHI 660D). The proof-of-concept device was fabricated by assembling the CCM thin film (0.2 cm × 1 cm) on a polystyrene foam substrate. The film was bent to a U-shape and bound on the polystyrene foam. The two terminals of the film were sealed by an Ag/AgCl gel electrode (60/40, Sigma-Aldrich) and then connected with graphite paper as conductive wires. The whole device was floated on an aqueous electrolyte (0.01 M NaCl, pH = 10) while half of the film was soaked in the electrolyte. The open-circuit voltage and the I-V curves of the device were collected by an electrochemical workstation (CHI 660D) and a source meter (Hewlett Packard 34401A), respectively.

## Supplementary Results and Discussion

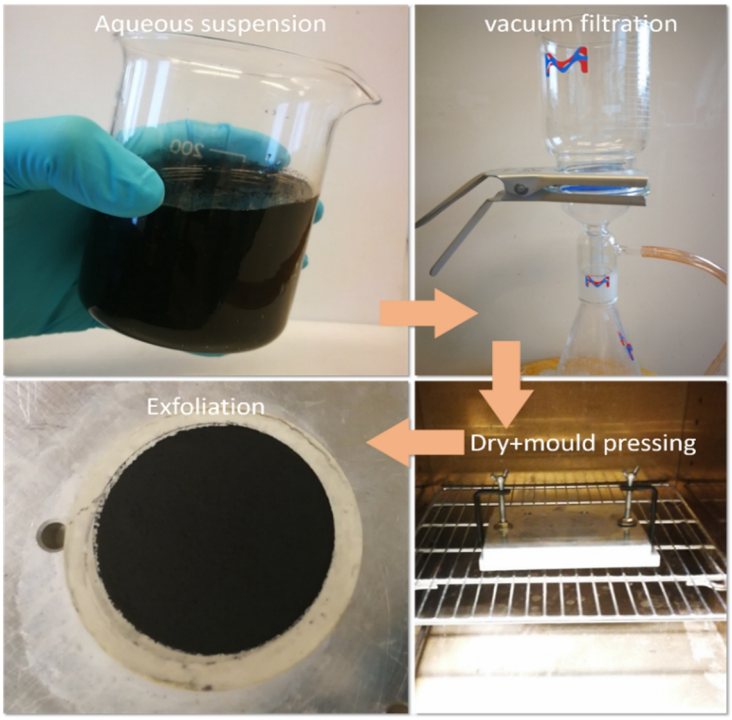


**Fig. S1**. Photos showing the preparation steps to fabricate the CCM films.

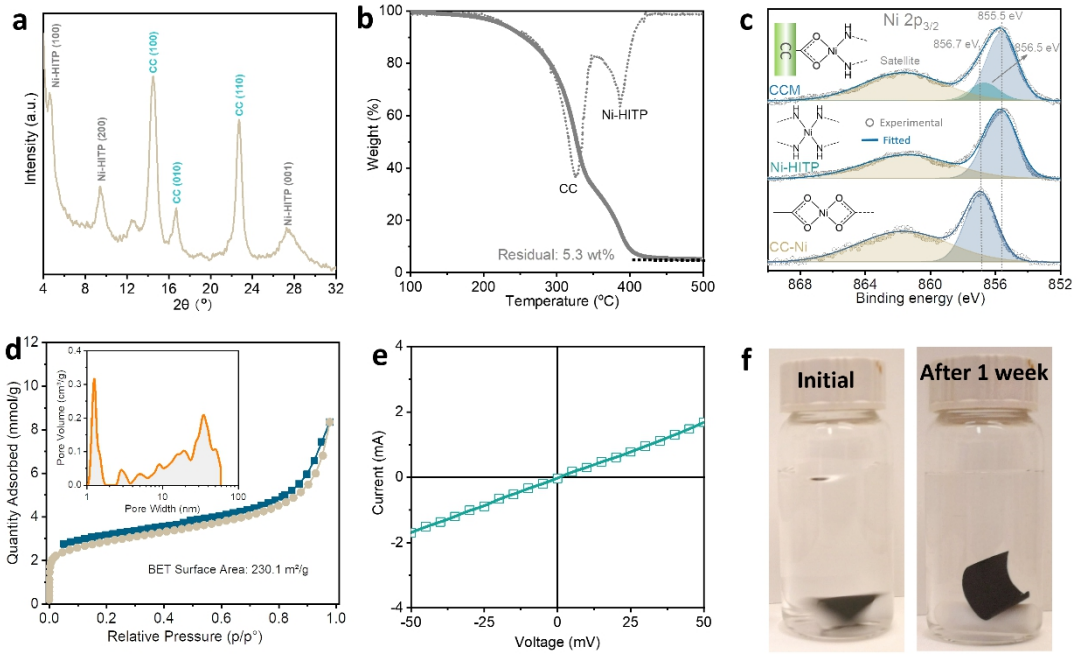


**Fig. S2**. Characterizations of CCM film. (**a**) XRD pattern of the CCM film. (**b**) The thermogravimetric analysis (TGA) curve of CCM film (oxygen). (**c**) Ni $2p_{3/2}$ X-ray photoelectron spectra of CCM, pure Ni−HITP, and CC−Ni ($Ni^{2+}$ ion-exchanged CC). (**d**) $N_2$ adsorption and desorption isotherms, calculated Brunauer–Emmett–Teller (BET) specific surface area and pore size distributions of the CCM film. (**e**) I-V curves of the CCM thin film. (**f**) Photos of CCM film in water during stirring (500 rpm) before and after 1 week in water.

The XRD pattern shows sharp diffraction peaks at 2θ ≈ 4.7 and 9.5°, corresponding to the (100) and (200) planes of the conductive MOF $Ni_3$(2,3,6,7,10,11−hexaiminotriphenylene)$_2$ (Ni-HITP). The broader peak at 2θ ≈ 27.6° can be attributed to the (001) reflection of the Ni-HITP. The peaks observed at 2θ ≈ 13.1°, 15.2°, 20.2° correspond to the (100), (010), (110) reflections, respectively, of cellulose nanofibers (Fig. S2a).

The TGA measurement of the CCM film was carried out under air atmosphere and the composition of the residue was determined to be NiO by XRD analysis. Therefore,

the analysis of the TGA curve indicates that the CCM film is composed of ~17.5 wt% Ni-HITP and 82.5wt% cellulose nanofibers (Fig. S2b).

The X-ray photoelectron spectroscopy (XPS) was employed to analyze the interfacial structure between the cellulose and the Ni-HITP (Fig. S2c). The binding energy of Ni $2p_{3/2}$ in CC-Ni (prepared by ion-exchange of $NiCl_2$ with carboxylated CC) was 856.7 eV, close to the value of nickel (II) acetate. This means that the Ni(II) species in the CC-Ni were coordinated by carboxylate groups on the surface of CC, similar to the coordination environment of Ni(II) in nickel (II) acetate. While the binding energy for the Ni(II) species in Ni-HITP negatively shifted to ~855.5 eV, where Ni(II) were coordinated by four amine groups. In comparison, the Ni $2p_{3/2}$ XPS spectrum of CCM can be deconvoluted into two peaks at 855.5 and 856.5 eV, which indicates the existence of two different chemical environments for Ni (II) in the CCM film. The peak at 855.5 eV can be assigned to Ni(II) in the Ni-HITP nanolayer, while the peak at 856.5 eV can be attributed to Ni(II) at the interface of the hybrid nanofiber bonding the CC and the Ni-HITP nanolayer. These results strongly suggest that the Ni-HITP nanolayers were chemically bonded to the surface of CC via an interfacial growth approach.

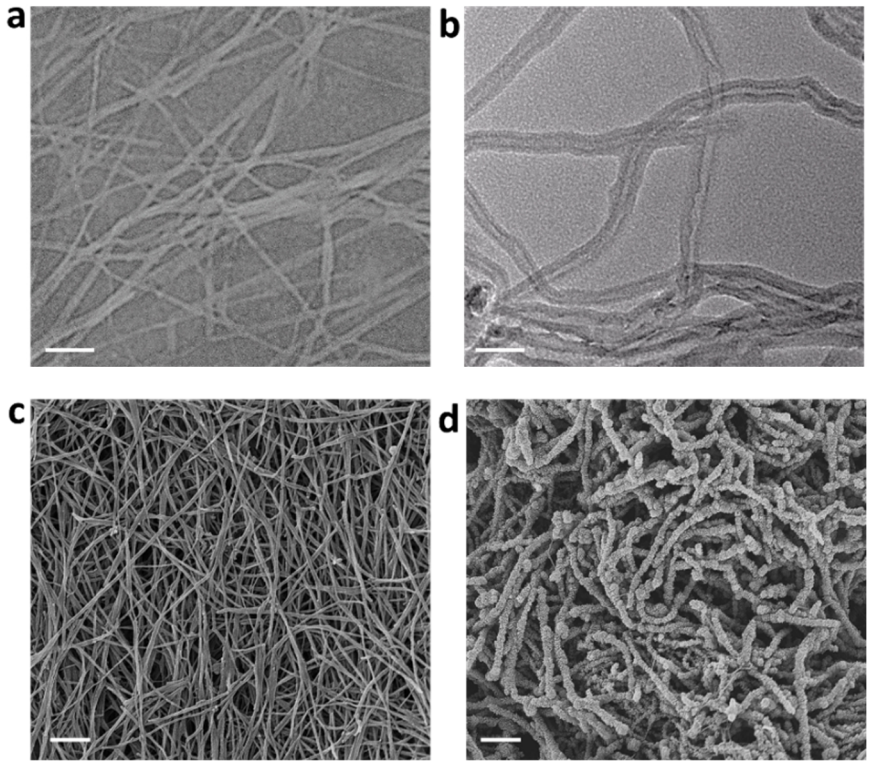


**Fig. S3**. TEM image of (a) pristine CC and (b) CCM; the scale bar: 100 nm. SEM image of (c) pristine CC and (d) CCM; the scale bar: 200 nm.

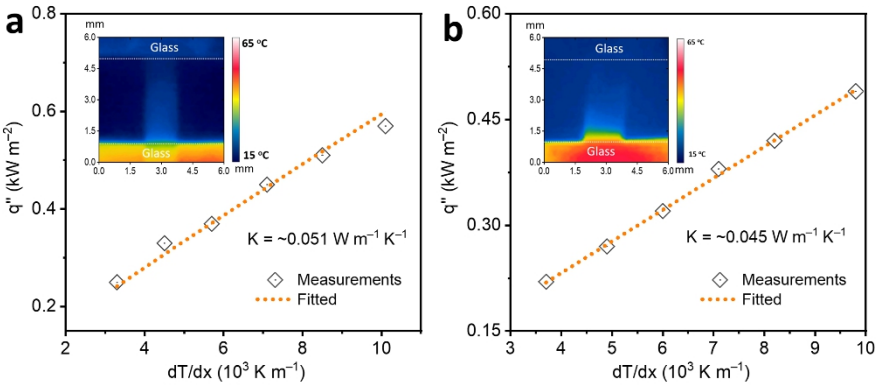


**Fig. S4**. Thermal conductivity of (**a**) pristine CC and (**b**) CCM film.

The in-plane thermal conductivities of the pure CC film and the CCM film were estimated as shown in Fig. S4.[4] The CC film and the CCM film both have low thermal conductivities of~0.04−0.05 W m$^{-1}$ K$^{-1}$, which are one order of magnitude lower than that of pure Ni-HITP (0.2 W m$^{-1}$ K$^{-1}$).[5] The low thermal conductivity of the CCM film can be attributed to its hierarchical porous structure and the hybrid composition. The abundant micropores and mesopores in the film could suppress gas movement while the hybrid structure of the film could scatter phonons. As a result, the synergetic effect resulted in relatively low thermal conductivity for the CCM film.

In addition to experimental measurement, we also theoretically calculated the thermal conductivity of the CCM film. Generally, conduction, radiation and convection contribute to the thermal conductivity of the film, where the latter two are negligible for isotropic porous materials at room temperature. Therefore, conduction, including gas conduction and solid conduction, is the main contributor to the overall thermal conductivity. The gas conductivity $\lambda_{gas}$ of the CCM film can be estimated from the equation:[6]

$$\lambda_{gas} = \frac{\lambda_{g0}\Pi}{1 + \frac{2\beta l_m}{\delta}}$$

where $\lambda_{g0}$ is the thermal conductivity of air (0.025 W m$^{-1}$ K$^{-1}$), $\Pi$ is the porosity (44.6 % of the CCM film, calculated based on its pore volume 0.28 cm$^3$ g$^{-1}$ and the bulk density 1.59 g cm$^{-3}$), $\beta \approx 2$ for air in a porous film, $l_m$ is the mean free path of air in specific pores. We estimate $l_m$ in the CCM film to 10 nm (versus 75 nm in free space), $\delta$ is the average diameter of the pores (2 nm for micropore and 35 nm for mesopores in CCM film). In this case, the $\lambda_{gas}$ can be calculated to be 0.021 W m$^{-1}$ K$^{-1}$. The solid conduction of the CCM film can be calculated by a weighted average of the effective solid conduction $\lambda^*_{solid}$ of the individual components.

$$\lambda^*_{solid} = \frac{\lambda_{solid}}{1 + \lambda_{solid}\frac{R_K}{d}}$$

where $d$ is the mean size, and $\lambda_{solid}$ is the solid conduction of the individual bulk components (0.05 W m$^{-1}$ K$^{-1}$ for cellulose, 0.2 W m$^{-1}$ K$^{-1}$ for Ni-HITP). $R_K$ is the interfacial thermal resistance, which value is assumed to be similar in magnitude to that for carbon nanotubes ($10^{-7}$ m$^2$ K W$^{-1}$).[7] Therefore, the $\lambda_{solid\ (CCM)}$ can be estimated to be 0.054 W m$^{-1}$ K$^{-1}$. The overall thermal conduction of the CCM film is: $\lambda = \lambda_{solid\ (CCM)} \times 55.4\ \% + \lambda_{gas} \times 44.6\ \% = 0.039$ W m$^{-1}$ K$^{-1}$.

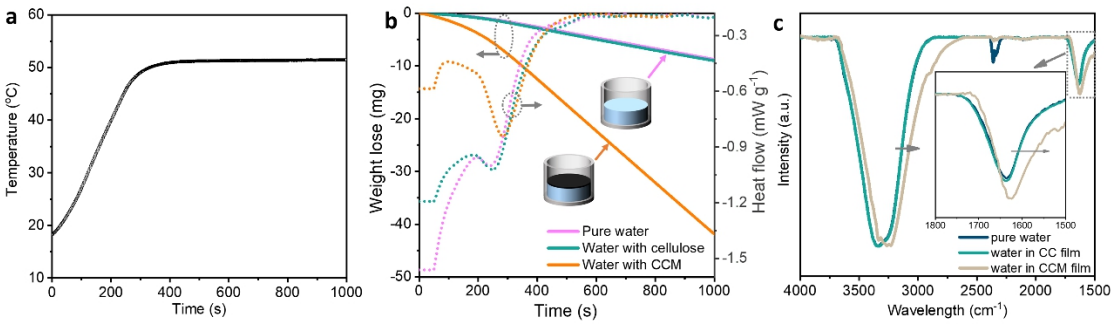


**Fig. S5**. Investigation of the mechanism of fast water evaporation by CCM film. (**a**) The temperature programming of TGA: first equilibrating at 17 ℃, then temperature increase with a rate of 5 K $min^{-1}$ until 53 ℃ to simulate the experimental rate, finally the temperature was stable at 53 ℃ for 30 min. (**b**). The simulated mass loss of water and corresponding enthalpy by TGA-DSC. (**c**) FTIR spectrum of pure water, water in CC film and CCM film (these two spectra were obtained by subtracting the background of CC film and CCM film).

In order to investigate the mechanism of the fast water evaporation facilitated by the CCM film, both thermal gravimetric analysis (TGA) and differential scanning calorimetry (DSC) were employed, where TGA was used to simulate the thermal evaporation process and DSC to monitor the enthalpy. By controlling the heating rate according to the experimentally measured value (Fig. S5a), the water mass loss under the CCM film was determined to be 2.2 kg $m^{-2}$ $h^{-1}$ (schematic of apparatus in Fig. S5b) which is close to the experimental result of 2.42 kg $m^{-2}$ $h^{-1}$. This demonstrates that the simulated TGA procedure is very similar to the actual evaporation process under one sun illumination. Hence, we can conclude that it required less enthalpy but higher temperature for water evaporation through the CCM film than without the film (Fig. S5b).[8] An experiment in which a hydrophilic cellulose film with mesopores covered a water surface was also carried for comparison. An almost similar mass-loss and enthalpy as for the set-up with pure water without a film on top was observed in this

case. These results suggest that the acceleration of water evaporation is caused by the nanopores of Ni-HITP reducing the vaporization enthalpy.

We also used Fourier transform infrared (FTIR) measurements to explore the molecular behavior of water in the CCM film by comparing the spectrum of pure water with the spectra of water underneath the CC film and the CCM film (Fig. S5c). The absorption bands at 3219 and 3373 $cm^{-1}$ correspond to the O−H symmetric stretching ($V_s$) and asymmetric stretching ($V_{as}$) modes of water, respectively. The bands of water in the CCM film are significantly red-shifted as compared to the band of pure water (3203 $cm^{-1}$ for $V_s$, 3369 $cm^{-1}$ for $V_{as}$), while no such shift was observed for the bands of water in the CC film. This suggests the water molecules tend to be more strongly bonded by hydrogen-bonds within the CCM film compared with the bonds in pure water. The absorption band observed in the lower wavelength range at 1639 $cm^{-1}$ are assigned to the H−O−H scissor mode of water molecule. A significant red-shift can be observed in the absorption band of water in the CCM film (1623 $cm^{-1}$) as compared to the corresponding band in pure water and water in the CC film (1636 $cm^{-1}$). These results indicate the formation of water clusters in CCM films.[9] Combined with the results of DSC-TGA, the fast water evaporation facilitated by the CCM film can be attributed to the water cluster confinement in the nanopores, which requires less vaporization enthalpy compared with the water without any confinement.

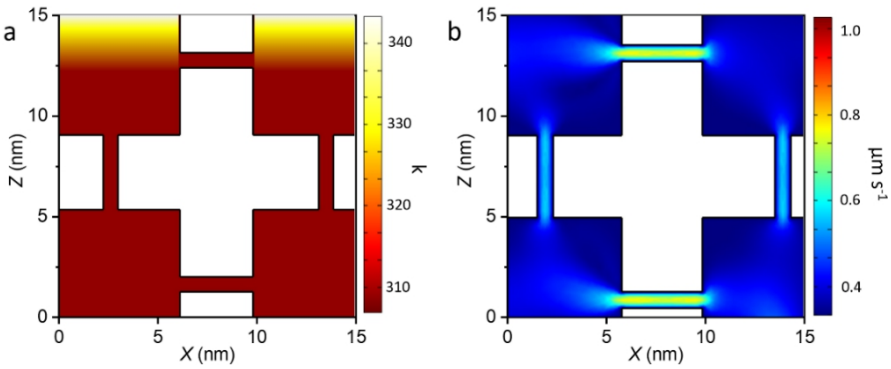


**Fig. S6**. COMSOL simulation of (**a**) temperature distribution and (**b**) water transport in CCM film induced by surface evaporation.

The water transport in the CCM film during the evaporation process was simulated by the COMSOL software. The porous structure of the CCM film was simplified into a two-dimensional interconnected network containing mesoporous and microporous channels with diameters of 20 and 2 nm, respectively (Fig. S6). The water loss rate from the upper boundary was set to 0.67 μm $s^{-1}$ that mimics the water evaporation rate of 2.42 kg $m^{-2}$ $h^{-1}$ in the CCM film under solar thermal steam generation process. The simulation results indicate that the nanoporous channels greatly facilitated the water transport. In addition, the water transport in the micropore channels is faster than that in mesoporous channels.

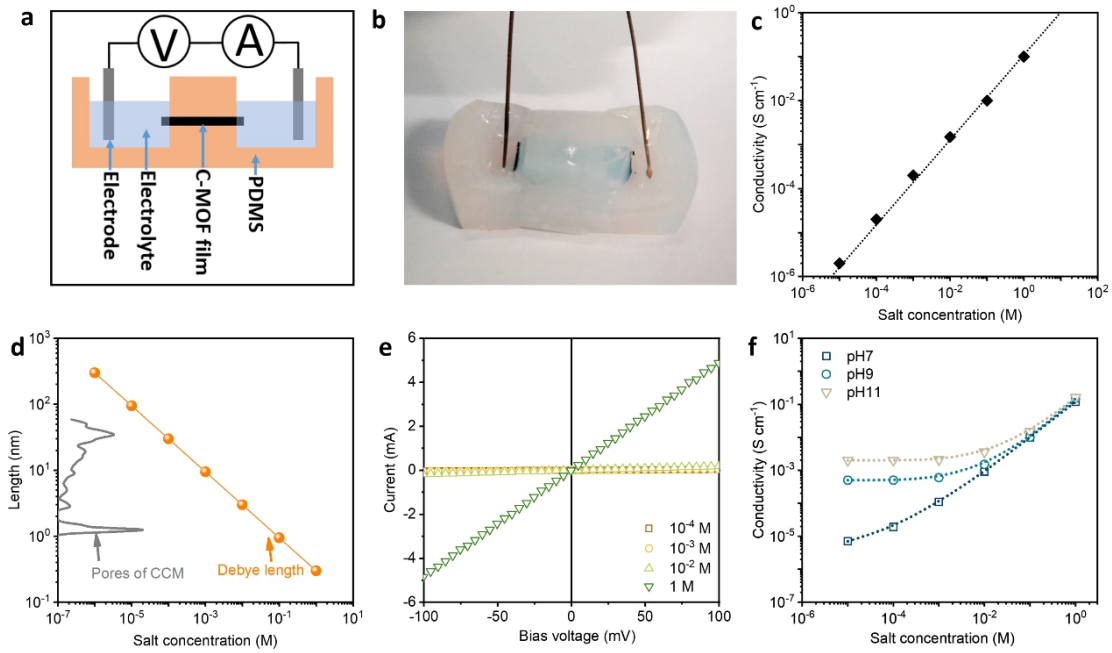


**Fig. S7**. (**a**) Schematic and (**b**) photo of the set-up for the measurement of ion conductivity of the CCM film along the in-plane direction.[3] (**c**) Measured ion conductivity of bulk NaCl solution with different salt concentration. (**d**) Comparison of the Debye length of electrolyte ions at different salt concentrations with the pore size distribution of the CCM film. (**e**) I-V curves obtained at different NaCl concentrations with a fixed pH value of 10. (**f**) The ion conductivity of the CCM film as a function of the NaCl concentration at pH values of 7, 9, and 11.

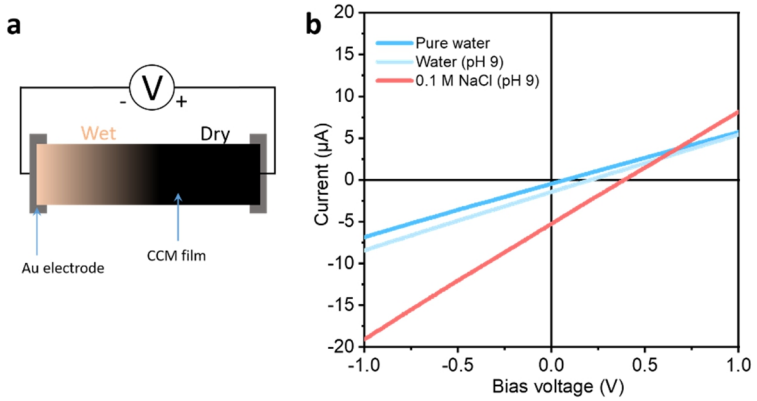


**Fig. S8**. (**a**) Schematic of the set-up for streaming potential measurements. (**b**) I-V curves collected by using different electrolytes.

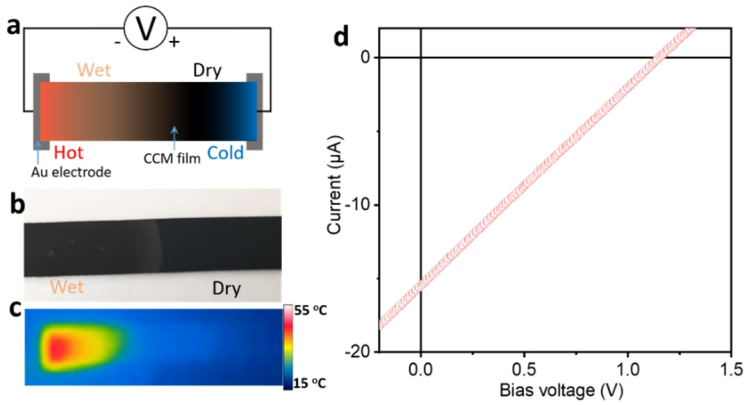


**Fig. S9**. (**a**) Schematic of the set-up for ionic potential measurements by exposing the wet side of the CCM film to one sun illumination. (**b**) Photo of the CCM film showing the wet-dry interface when dropping the electrolyte onto one side of the film. (**c**) IR image of the set-up showing the temperature distribution on the CCM film by exposing the wet side of the film to one sun illumination. (**d**) I-V curve collected by exposing the wet-side of CCM to one sun illumination after 10 min.

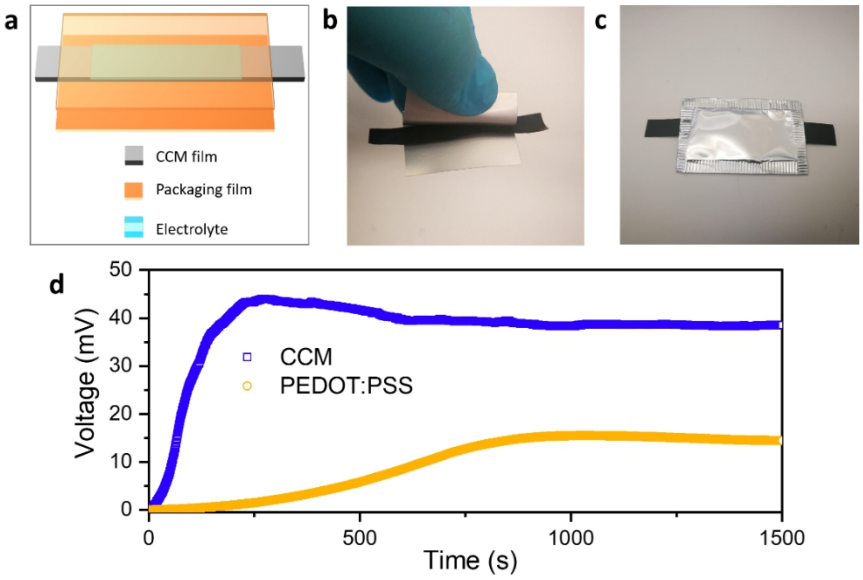


**Fig. S10**. (**a**) Schematic of the home-made device for the ionic thermoelectric voltage measurements. Photo of (**b**) a detached and (**c**) a sealed device. (**d**) The measured open-circuit voltage (ion thermoelectric voltage) of the CCM film and the PEDOT:PSS[10] film under a temperature gradient of 5°C between the two sides of the film (17 vs 22°C). The ionic Seebeck coefficient of the film can be calculated according to the equation $S = \Delta V/ \Delta T$. The ionic Seebeck coefficient of the PEDOT:PSS film was calculated to be around 3.05 mV $K^{-1}$, close to the reported value (3.3 mV $K^{-1}$),[11] indicating the feasibility of the measurement method.

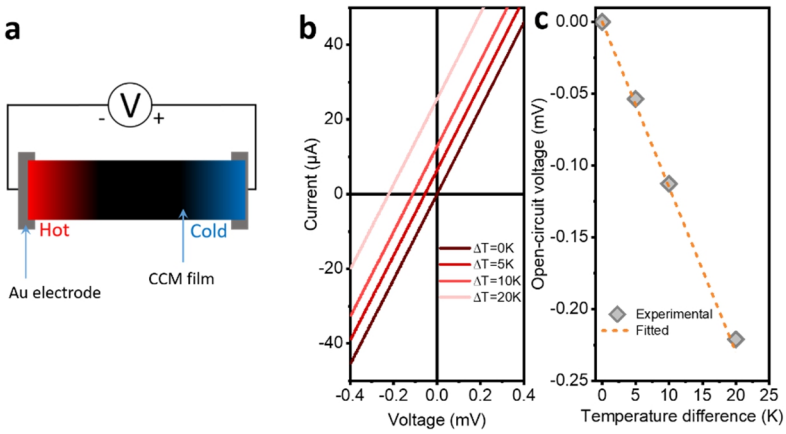


**Fig. S11**. (**a**) Schematic of the set-up for the measurement of electronic *Seebeck* coefficient. (**b**) I-V cures recorded at different temperature gradients. (**c**) Plot of the open-circuit voltage versus temperature gradients.

The electronic *Seebeck* coefficient ($\alpha_e$) is defined as:[11]

$$S = \Delta V / \Delta T$$

where $\Delta V$ is the open-circuit voltage, $\Delta T$ is the temperature gradient. Exposing only one side of a dry CCM film for different intervals to one sun illumination can generate different thermal gradients (Fig. S11a). Meanwhile, the open-circuit voltage was measured as shown in Fig. S11b. By plotting the voltage vs. temperature gradient, the $\alpha_e$ value was determined to be −11.5 μV $K^{-1}$ by measuring the slope of the plot (in Fig. S11c). The calculated value is close to the reported $\alpha_e$ value of Ni-HITP.[5]

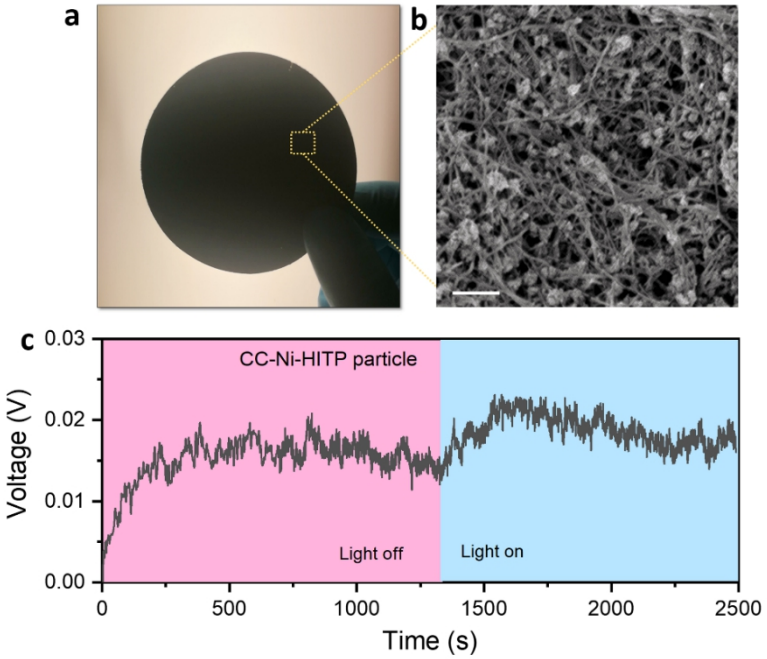


**Fig. S12**. (**a**) Photo and (**b**) SEM image of the CC-Ni-HITP nanopaper prepared by direct blending the CC with Ni-HITP particles (scale bar: 1 μm). (**c**) Measured open-circuit voltage of the CC- Ni-HITP nanopaper over time with and without light illumination (one sun).

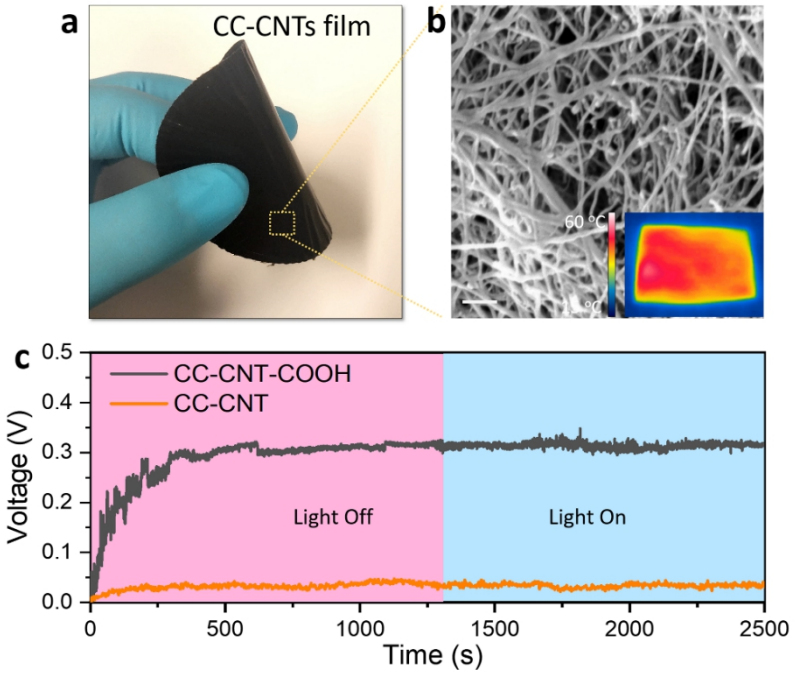


**Fig. S13**. (**a**) Photo and (**b**) SEM image of the CC-CNTs nanopaper prepared by direct blending the CC with CNTs (scale bar: 200 nm). The infrared image shows the temperature distribution on the surface after illumination for 20 min. (**c**) Measured open-circuit voltage of the CC-CNT film over time with and without light illumination (one sun).

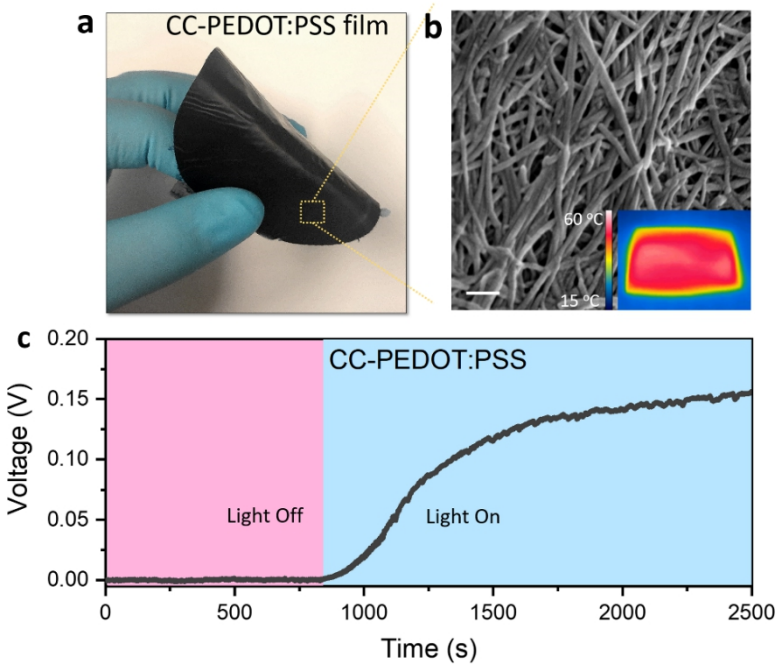


**Fig. S14**. (**a**) Photo and (**b**) SEM image of the CC@PEDOT:PSS film prepared by direct blending the CC with PEDOT:PSS (scale bar: 200 nm). The infrared image shows the temperature distribution on the surface after illumination for 20 min. (**c**) Measured open-circuit voltage of the CC@PEDOT:PSS film over time with and without light illumination (one sun).

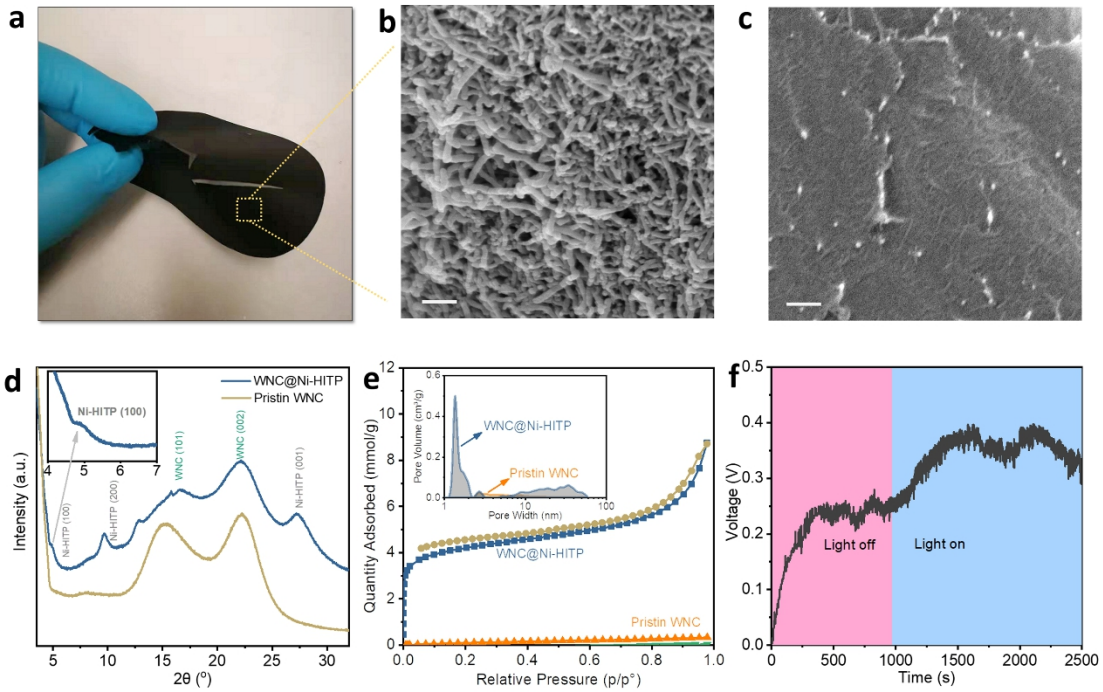


**Fig. S15.** (a) Photograph and (b) SEM image of the wood nanocellulose (WNC) @ Ni-HITP film; the scale bar: 200 nm. (c) SEM image of pristine wood nanocellulose. (d) X-ray diffraction analyses of the WNC@Ni-HITP and the pristine WNC film. (e) $N_2$ adsorption and desorption isotherms of the WNC@Ni-HITP and the pristine WNC film. The inset shows the pore size distribution in the films calculated from the adsorption branches (f) Measured open-circuit voltage of the WNC@Ni-HITP film over time with and without light illumination (one-sun).

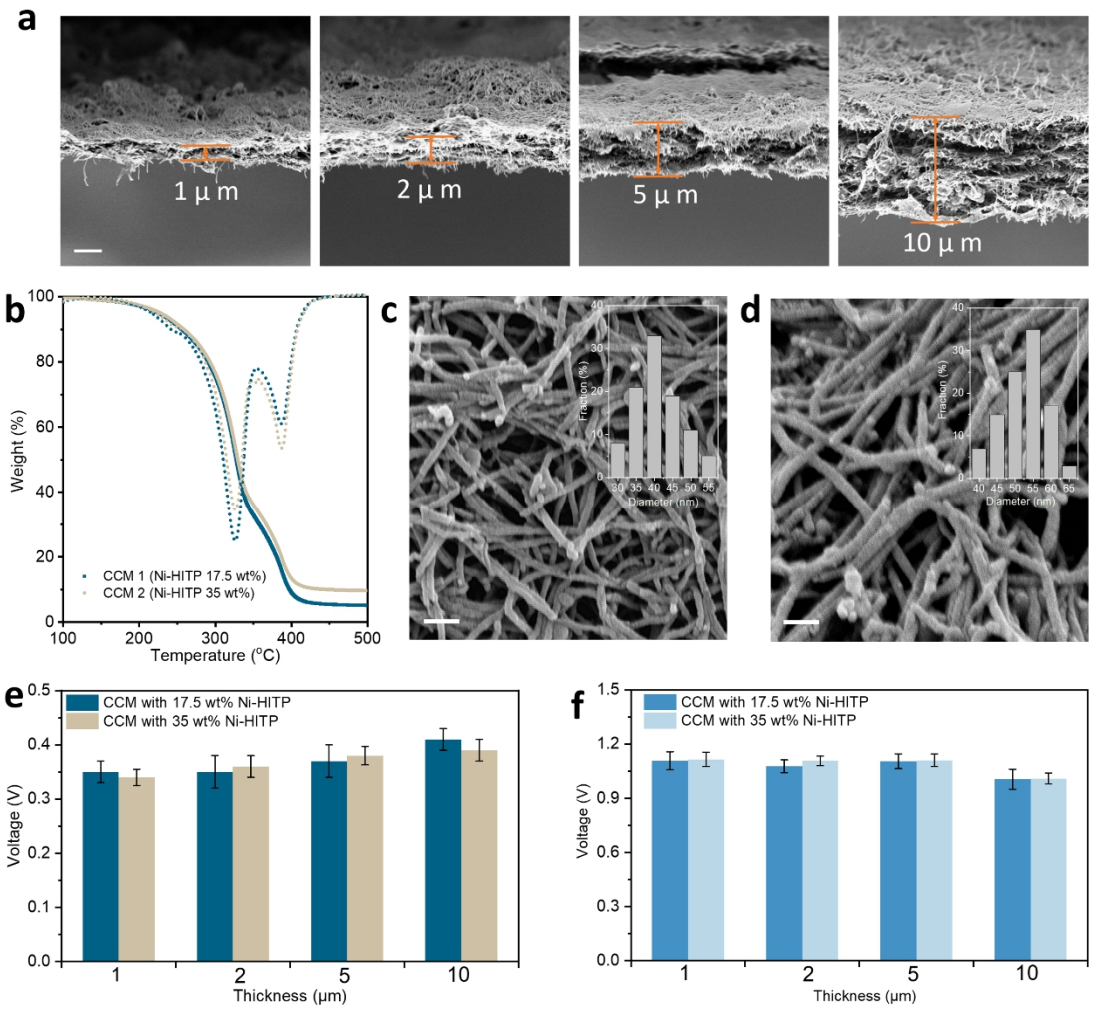


**Fig. S16**. Investigation of the effect of composition and thickness of the CCM film on the voltage output. (a) Cross-sectional SEM images of the CCM films with different thicknesses. (b) TGA curves of CCMs film with different compositions. SEM image and diameter distribution of CCM hybrid nanofiber with (c) 17.5 wt% Ni-HITP and (d) 35 wt% Ni-HITP, the scale bar: 200 nm. A comparison of the (e) streaming potentials (under ambient conditions) and (f) overall voltage output (under one sun illumination) generated in the CCM films with different compositions and thicknesses.

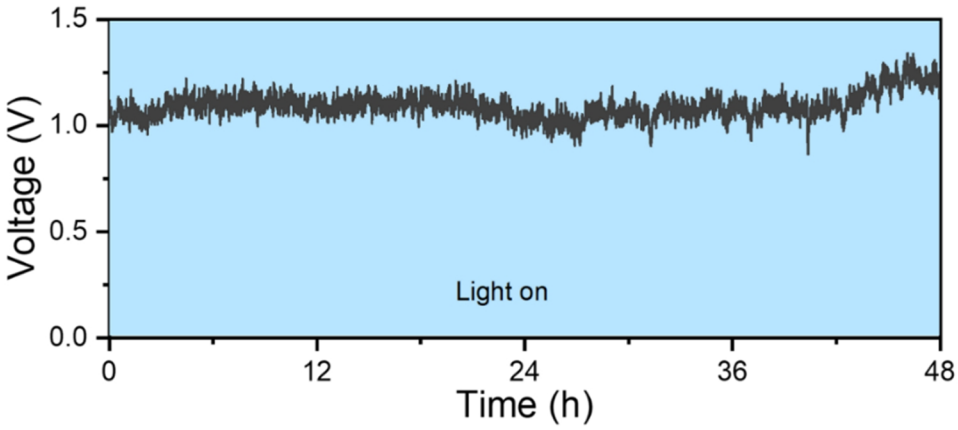


**Fig. S17**. Measured open-circuit voltage of a CCM film device under one sun illumination for 48 h.

**Table S1**. A summary of reported systems for solar thermal steam generation.

| Materials | Evaporation rate ($kg\ m^{-2}\ h^{-1}$) | Light intensity ($kW\ m^{-2}$) | Ref. |
|---|---|---|---|
| Polypyrrole film | 1.45 | 1 | Adv. Mater. 2019, 31, 1807716 |
| Carbon nanotube | 1.3 | 1 | Adv. Mater. 2017, 29, 1700981 |
| Au nanoparticle | 0.5 | 1 | Nat. Commun. 2015, 6, 10103 |
| Polypyrrole hydrogel | 4 | 1 | Energy Environ. Sci. 2020, 13, 2087-2095 |
| Cu-HHTP MOF | 1.5 | 1 | Adv. Mater. 2019, 31, 1808249 |
| $MoS_2$ | 1 | 1 | Adv. Funct. Mater. 2018, 28, 1704505 |
| $MoS_2$ nanosheets | 2.5 | 1 | Adv. Mater. 2020, 32, 2001544 |
| Titania nanoparticle | 0.8 | 1 | Adv. Energy Mater. 2017, 7, 1601811 |
| Mxene | 1.1 | 1 | ACS Nano 2017, 11, 3752-3759 |
| Graphene | 1.7 | 1 | Adv. Mater. 2015, 27, 4302–4307 |
| Nanoporous $MoS_2$ | 2.5 | 1 | Adv. Mater. 2020, 32, 2001544 |
| Nanoporous hydrogel | 4.0 | 1 | Energy Environ. Sci. 2020, 13, 2087-2095 |
| Multistage device | 5.78 | 1 | Energy Environ. Sci. 2020, 13, 830-839 |
| 3D cup-shaped $CuFeMnO_4$ | 2.04 | 1 | Joule 2018, 2, 1171-1186. |
| Nanoporous PPy + PVA | 3.4 | 1 | Nat. Nanotech. 2018, 13, 489-495. |
| Photovoltaics membrane | 2.0 | 1 | Nat. Commun. 2019, 10, 3012. |
| PPy-stainless steel mesh | 1.8 | 1 | Adv. Mater. 2015, 27, 4889-4894 |
| CCM film | 2.42 | 1 | This work |

**Table S2.** Comparison of power generation systems based on reverse electrodialysis, streaming potential and ionic thermophoresis effects.

| Materials | Mechanism | Voltage | Electrolyte | Ref. |
|---|---|---|---|---|
| $MoS_2$ single nanopore | Reverse electrodialysis | 0.2 V | 1 M/1 mM KCl | Nature 2016, 536, 197-200 |
| Silk membrane | Reverse electrodialysis | 0.1 V | 1 M/1 mM KCl | Nat. Commun. 2019, 10, 3876 |
| Mxene membrane | Reverse electrodialysis | 0.1 V | 1 M/1 mM KCl | Nat. Commun. 2019, 10, 2920 |
| Black phosphorus | Reverse electrodialysis | 0.2 V | 1 M/1 mM KCl | PNAS 2020, 117, 13959-13966 |
| Carbon black | Streaming potential | 1.5 V | Pure water | Nat. Nanotechnol. 2017, 12, 317-321 |
| Carbon black | Streaming potential | 0.7 V | 1M $CaCl_2$ | Energy Environ. Sci., 2020, 13, 527-534 |
| AlOOH/UIO-66 nanosheet | Streaming potential | 1.8 V | Pure water | Adv. Mater. 2020, 32, 2003720 |
| Copper nanowire | Streaming potential | 0.5 V | 0.01M NaCl | Energy Environ. Sci. 2020, 13, 3432-3438 |
| Protein nanowires | Streaming potential | 0.8 V | Pure water | Nature 2020, 578, 550-554 |
| PEO gel | Ion thermophoresis | 11 mV/K | 3 wt% NaOH | Energy Environ. Sci. 2016, 9, 1450-1457 |
| Nanochannel simulation | Ion thermophoresis | 9 mV/K | 0.35M NaCl | Phys. Rev. Lett. 2019, 123, 138001 |
| Wood | Ion thermophoresis | 24 mV/K | 0.625M NaOH | Nat. Mater. 2019, 18, 608-613 |
| Gelatin | Ion thermophoresis | 17 mV/K | 0.8 M KCl | Science 2020, 368, 1091-1098 |
| CCM film | Streaming potential + Ion thermophoresis | 1.1 V | 0.01 M NaCl | This Work |

**Table S3**. Power density of reported ionic power generators.

| Material | Driving force | Electrode | Power density | Ref. |
|---|---|---|---|---|
| Mxene | Salinity gradient | Ag/AgCl | 2.7 W $m^{-2}$ | Nat. Commun. 2019, 10, 2920 |
| Silk | Salinity gradient | Ag/AgCl | 3.5 W $m^{-2}$ | Nat. Commun. 2019, 10, 3876 |
| Wood | Thermal gradient | Pt | - | Nat. Mater. 2019, 18, 608-613 |
| Mxene | Thermal gradient + Salinity gradient | Ag/AgCl | 2.5 W $m^{-2}$ | ACS Nano 2020, 14, 9042-9049 |
| GO | Streaming | Al | 1 mW $m^{-2}$ | Energy Environ. Sci. 2016, 9, 912-916 |
| Carbon black | Streaming | Carbon | - | Nat. Nanotechnol. 2017, 12, 317-321 |
| Si | Streaming | Ag/AgCl | 7.7 W $m^{-2}$ | Nano Lett. 2007, 7, 1022-1025 |
| Nafion | Thermal gradient | Ag/AgCl | 1 W $m^{-2}$ | Energy Environ. Sci. 2017, 10, 1923-1927 |
| CCM film | Streaming+ Thermal gradient | Ag/AgCl | 15 W $m^{-2}$ | This Work |

# References


1. T. Saito, S. Kimura, Y. Nishiyama and A. Isogai, *Biomacromolecules*, **2007**, 8, 2485-2491.
2. X. Li, G. Ni, T. Cooper, N. Xu, J. Li, L. Zhou, X. Hu, B. Zhu, P. Yao and J. Zhu, *Joule*, **2019**, 3, 1798-1803.
3. S. Qin, D. Liu, G. Wang, D. Portehault, C. J. Garvey, Y. Gogotsi, W. Lei and Y. Chen, *J. Am. Chem. Soc.*, **2017**, 139, 6314-6320.
4. H. Ghasemi, G. Ni, A. M. Marconnet, J. Loomis, S. Yerci, N. Miljkovic and G. Chen, *Nat. Commun.,* **2014**, 5, 4449.
5. L. Sun, B. Liao, D. Sheberla, D. Kraemer, J. Zhou, E. A. Stach, D. Zakharov, V. Stavila, A. A. Talin, Y. Ge, M. D. Allendorf, G. Chen, F. Léonard and M. Dincă, *Joule*, **2017**, 1, 168-177.
6. X. Lu, M. Arduini-Schuster, J. Kuhn, O. Nilsson, J. Fricke and R. Pekala, *Science*, **1992**, 255, 971-972.
7. (a) Z. Han and A. Fina, *Prog. Polym. Sci.*, 2011, 36, 914-944; (b) B. Wicklein, A. Kocjan, G. Salazar-Alvarez, F. Carosio, G. Camino, M. Antonietti and L. Bergström, *Nat. Nanotechnol*., **2015**, 10, 277-283.
8. F. Zhao, X. Zhou, Y. Shi, X. Qian, M. Alexander, X. Zhao, S. Mendez, R. Yang, L. Qu and G. Yu, *Nat. Nanotechnol*., **2018**, 13, 489-495.
9. N. Nijem, P. Canepa, U. Kaipa, K. Tan, K. Roodenko, S. Tekarli, J. Halbert, I. W. Oswald, R. K. Arvapally, C. Yang, T. Thonhauser, M. A. Omary and Y. J. Chabal, *J. Am. Chem. Soc.*, **2013**, 135, 12615-12626.
10. S. Zhou, Z. Qiu, M. Strømme and Z. Wang, *Adv. Funct. Mater*., **2020**, 30, 2005757.
11. H. Wang, U. Ail, R. Gabrielsson, M. Berggren and X. Crispin, *Adv. Energy Mater.*, **2015**, 5, 1500044.